Procedia Manufacturing

Volume 5, 2016, Pages 838–848

44th Proceedings of the North American Manufacturing Research Institution of SME http://www.sme.org/namrc

Experimental Investigation of the Grinding Force in Rotational Atherectomy

Yihao Zheng[1*], Yang Liu[1], Yao Liu[1], and Albert J. Shih[1]
[1]*The University of Michigan, Ann Arbor, U.S.A.*
yhzheng@umich.edu, yliume@umich.edu, yaoliuz@umich.edu, shiha@umich.edu

Abstract
Rotational atherectomy, a catheter-based procedure, utilizes an ellipsoidal diamond abrasive grinding wheel to remove the calcified atherosclerotic plaque from the artery and restore the blood flow for the treatment of the occlusive cardiovascular disease. Complications of rotational atherectomy, including dissection, perforation, re-stenosis, and slow-flow/no-reflow, could be related to the grinding force on the artery. This study measures the grinding force in rotational atherectomy using the piezoelectric dynamometer on tissue-mimicking phantom models with or without a ring-shape bovine bone workpiece as the surrogate to the calcified plaque. The difference in force measurements on these two phantom models is due to the plaque grinding force. With the grinding wheel rotational speed ranging from 135 to 175 kRPM, this difference varied from 40.9 to 63.3 mN. The same orbital speeds between these two phantoms were observed at each rotational speed. This study establishes the foundation to understand the rotational atherectomy grinding mechanism.

Keywords: Grinding force, Tissue phantom, Rotational atherectomy, Cardiovascular disease

1 Introduction

Occlusive cardiovascular disease, the number one cause of death in the US (National Vital Statistics Report, 2013), is caused by atherosclerosis, the accumulation of fatty and calcified plaque on the arterial wall, restricting the blood flow. To open the plaque blockage in the artery, about 600,000 angioplasty procedures are performed every year in the US (Fang et al., 2013) to compress the plaque into the vessel wall by balloon dilating and stent bracing inside the lesion via a catheter. Angioplasty is ineffective in severely calcified plaque, arterial bifurcation, ostial stenosis, and in-stent restenosis (Morii and Miyazaki, 2014; Quevedo et al., 2012; and Wasiak et al., 2000). To address these complex lesions, the rotational atherectomy (RA), as shown in Figure 1, removes the plaque by a diamond

* Corresponding author

 Selection and peer-review under responsibility of the Scientific Programme Committee of NAMRI/SME

doi:10.1016/j.promfg.2016.08.069

abrasive grinding wheel in the diseased artery. The grinding wheel is driven by a drive shaft which rotates between the stationary guidewire (0.23 mm diameter) and the sheath at a high speed (up to 210,000 rpm). Saline flowing through the sheath provides lubrication and cooling.

RA has been in use clinically for over 25 years since it was developed in the late 1980s (Ritchie and Hansen, 1987). Extensive clinical studies have been conducted to study RA techniques. Some of the recommendations are related to plaque grinding. Safian et al. (2001) and Whitlow et al. (2001) suggested that the rotational speed decrease during the procedure should be lower than 5,000 RPM. Excessive decrease of the speed indicated a large grinding force that might damage the healthy tissue or produce large size debris, which could block micro-vessels. The grinding wheel diameter was suggested to be smaller than 70% of the treated artery diameter to reduce the grinding force. Kini et al. (1999) recommended a short lesion engagement time of 20 to 30 s, to avoid excessive heat accumulation. Lin et al. (2013) and Dahdouh et al. (2013) provided mechanism and management of grinding wheel entrapment. Advancing the grinding wheel across a long, angulated and heavily calcified lesion may cause an excessive decrease of the rotational speed and the wheel entrapment. Pecking motion of the wheel and less than 15 s grinding time were recommended to avoid the entrapment. Barboto et al. (2015) published a universally accepted RA protocol, suggesting an initial grinding wheel size of 1.25 to 1.5 mm and a rotational speed ranging from 135 to 180 kRPM.

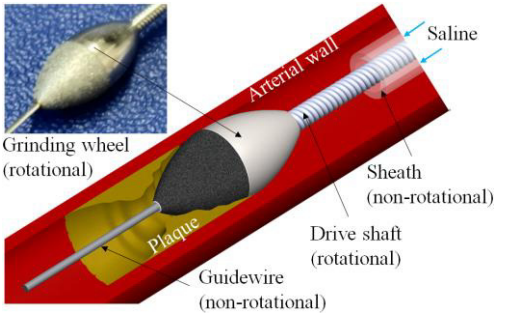

Figure 1: Schematic of RA mechanism of action.

Complications of RA were reported in these clinical studies. Major adverse cardiovascular events include death, myocardial infarction, and target lesion revascularization. Target lesion revascularization is often caused by re-stenosis, the regrowth of the plaque after RA. The re-stenosis rate could be over 50% (Hoffmann et al., 1998; Reifart et al., 1997; and Vom Dahl et al., 2002), which is very high. Angiographic complications (dissection, perforation, acute closure, and side branch loss), slow-flow/no-reflow, vasospasm, and grinding wheel entrapment were observed clinically in RA.

Engineering studies were conducted on RA to address these complications. Two novel grinding wheel designs were investigated: (1) Kim et al. (2011) utilized laser engraving for grinding wheel surface modification to avoid microcavitation and healthy tissue damage and (2) Nakao et al. (2005) created grater-like micro-blades on the wheel surface as the substitute to the diamond abrasives. Liu et al. (2016) examined the debris size distribution and ground surface morphology. Reisman et al. experimentally investigated the thermal injury (1998a) and platelet aggregation (1998b) with respect to the grinding wheel rotational speeds. This literature review indicates a lack of understanding in the RA grinding force.

Grinding force is fundamental to study the material removal mechanism, heat generation, and debris size in RA. Excessive grinding force may lead to vessel dissection, perforation, spasm, oversized debris, and tissue thermal damage. The high speed rotating grinding wheel surrounded by the blood inside the vessel is subject to the grinding force (due to abrasive-plaque interaction) and hydrodynamic force (due to the fluid pressure between the wheel and vessel wall). It is a technical challenge to distinguish these two forces. To identify the grinding force, this study presents a new approach to measure the force difference (using the piezoelectric force dynamometer) of two phantoms undergoing RA with the same geometry, one with and another without a ring-shaped bone to simulate the plaque (Demer and Tintut, 2008).

In this paper, the experimental setup, phantom fabrication, and design of experiments are first introduced. Results of the force measurement are then presented, followed by a discussion on the grinding force and investigation of the rotational speed effect.

2 Materials and Methods

2.1 Experimental Setup

The experimental setup, as presented in Figure 2, consists of three modules: the rotational atherectomy device, the tissue phantom, and the force measurement unit.

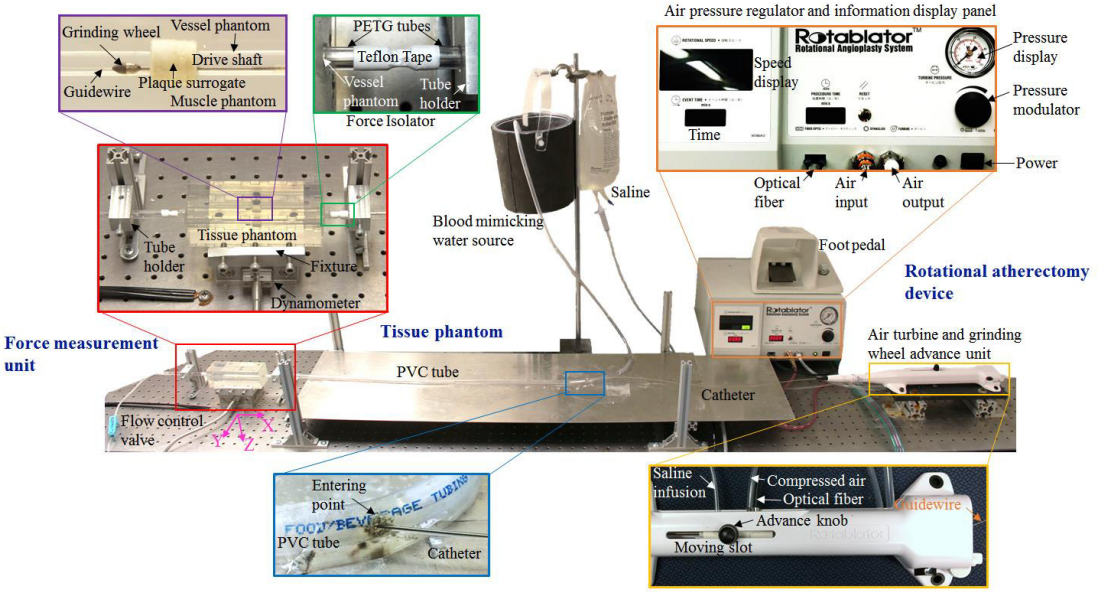

Figure 2: Experimental setup.

2.1.1 Rotational Atherectomy Device

The RA device, Rotablator™ by Boston Scientific (Marlborough, MA), consists of a catheter, an air turbine and grinding wheel advance unit, and an air pressure regulator with information display panel.

Catheter, as shown in Figure 3, is inserted into a patient's artery during RA. The catheter is inserted into a PVC tube, which represents the blood vessel in the experiment. Inside the PVC tube is the catheter. The blood mimicking water (37°C water) flows in between the catheter and PVC tube and the saline flows inside the catheter. The catheter includes a stainless steel guidewire (0.23 mm diameter), a drive shaft(0.65 mm outer diameter (OD), and a sheath (1.43 mm OD, 0.2 mm thick). The stationary guidewire extends from the air turbine through the drive shaft and grinding wheel to beyond the plaque (Figure 1). The guidewire serves as a rail which grinding wheel and drive shaft rotate around. Around the guidewire is the drive shaft as illustrated in the cross-section A-A in Figure 3. The drive shaft connects the grinding wheel and air turbine and is made of three helically wound 0.18 mm diameter stainless steel coils. The drive shaft rotates inside a stationary Teflon sheath. The friction between the drive shaft and the stationary guidewire and sheath is reduced by saline flowing between the sheath and guidewire during RA. The grinding wheel, as shown in Figure 3, is a nickel plated brass ellipsoid with the half distal to the drive shaft coated with diamond abrasives. As shown

in the scanning electron microscope (SEM) image of the abrasive coating, the size of the abrasives is about 10 μm. A 2.5 mm diameter grinding wheel was used for this study.

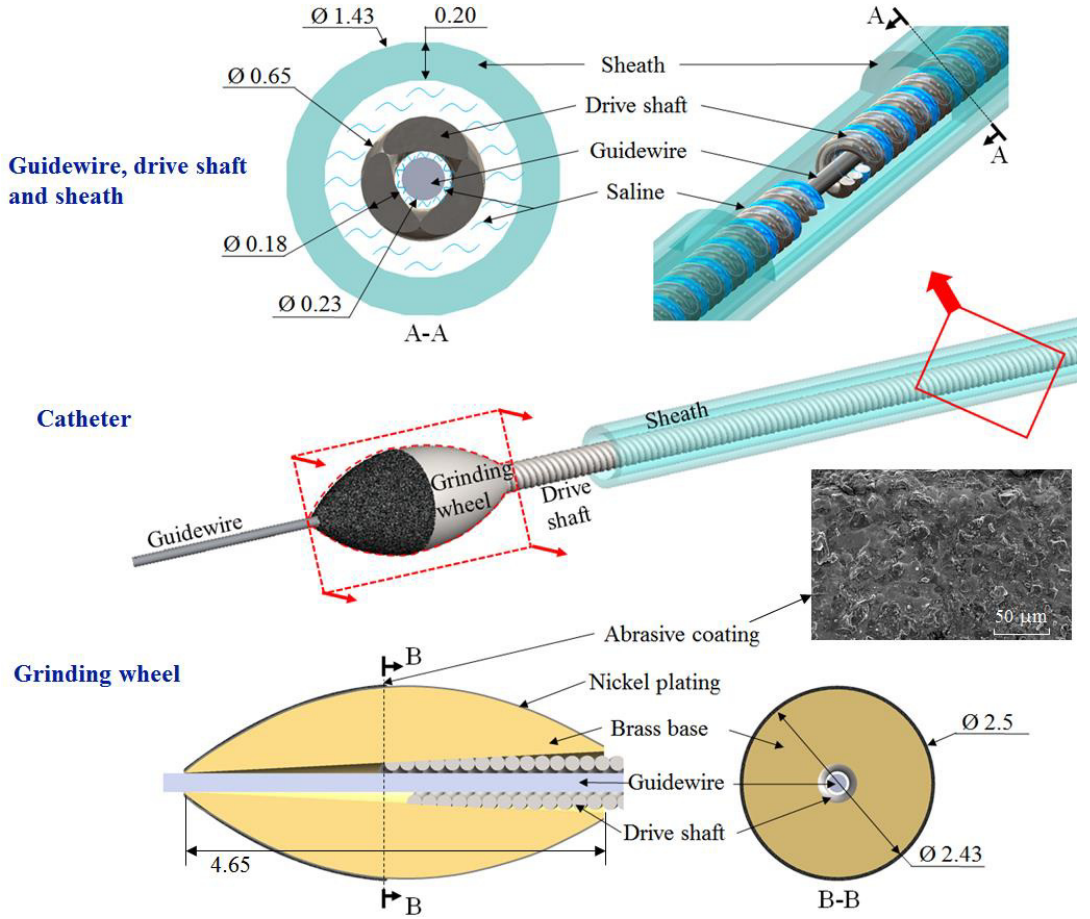

Figure 3: RA catheter components and dimension. (unit: mm)

The air turbine drives the grinding wheel from 6,000 to 210,000 PRM. An advance knob enables the manual movement of the grinding wheel in the axial direction, as shown in Figure 2. An air pressure regulator regulates the compress air to control the rotational speed of the grinding wheel.

2.1.2 Tissue Phantom

The tissue phantom was built to simulate the blood flow in the artery (Zheng et al., 2015). Two tissue phantoms, denoted as Phantom B and Phantom P, as shown in Figure 4(a) and (b), respectively, were designed and fabricated. Figure 4(c) shows the Phantom B during fabrication. A ring-shape bovine femur bone (4 mm ID, 6.6 mm OD and 8 mm in length) was the surrogate of the calcified plaque. This ring bone was put on a 4 mm aluminum rod. This bone-on-rod assembly was dip into the PVC liquid to dip coat a 2 mm thick PVC with the 45 kPa Young's modulus as the blood vessel. This coated aluminum rod was vertically held in a square shell (45×45×135 mm in size and 3.2 mm thick acrylic) with the bone part placed in the middle, as shown in Figure 4(c). The soft PVC was poured in the square shell filling the space between the shell and the coated rod. This PVC (8 kPa Young's modulus) was softer and mimicked the muscle phantom. The aluminum rod was removed after the PVC was cured and left a channel in the phantom as the blood vessel. The fabrication process of the

Phantom P was similar. The aluminum rod was coated without the bone part. A section of the vessel (hard) PVC coating was wrapped with the Teflon tape to ensure the same inner diameter as that of the Phantom B during RA.

A PVC tube (9.53 mm OD and 1.59 mm wall thickness) connects the water source and the tissue phantom. It has a hole to allow the catheter to enter the tube and access the tissue phantom. The blood mimicking water source was raised 1 m above the phantom (as shown in Figure 2) to regulate the water flow though the PVC tube and the tissue phantom at 40 mL/min flow rate (Farb et al., 1995). The saline bag is also at the same height to the phantom with 45 mL/min flow rate through the catheter.

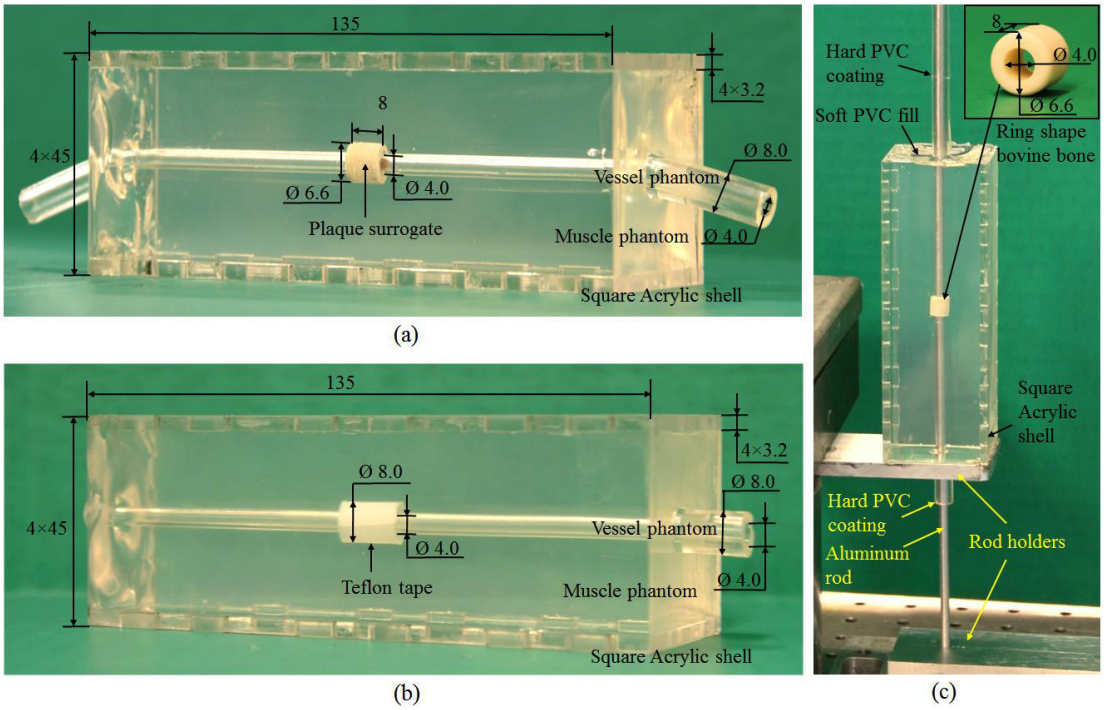

Figure 4: (a) Phantom B, (b) Phantom P, and (c) fabrication setup. (unit: mm)

2.1.3 Force Measurement Unit

Inside the tissue phantom, the grinding wheel rotated and the force on the phantom was measured by a piezoelectric force dynamometer (Model 9256C by Kistler) mounted underneath the tissue phantom via a custom fixture, as shown in Figure 2. To avoid the gravity effect, force in Y-direction as indicated in Figure 2 was measured. In Y-direction, this dynamometer has a natural frequency of 5,500 Hz (Kistler, 2003). To isolate the noise from the PVC tube induced by the vibration of the catheter, force isolators were implemented on both sides of the tissue phantom, as shown in Figure 2. The force isolator consisted of two adjacent polyethylene terephthalate (PETG) tubes (7.94 mm outer and 4.76 mm inner diameter) with a 5 mm gap. A Teflon tape was wrapped around the gap to create a flexible connection for isolating the force on the arterial phantom from two connecting PVC tubes. The grinding force was recorded at a sampling frequency of 5,000 Hz for four seconds. High frequency noise was removed by a low pass filter with a cut-off frequency of 2,100 Hz. The sensor drift was removed by eliminating the linear trend of the signal.

2.2 Film Thickness

The grinding wheel rotation in the blood mimicking water generates an elastohydrodynamic film. The film thickness, H, can be calculated by Equation (1) (Hamrock et al., 2004):

$$H = 7.43RU^{0.65}W^{-0.21}(1 - 0.85e^{-0.31}) \quad (1)$$

where

$$R = (\frac{1}{r_c} + \frac{1}{r_m})^{-1}, \quad U = \frac{V\mu_0}{E'R}, \quad W = \frac{w}{E'R^2}$$
$$V = \sqrt{u_c^2 + u_m^2}, \quad E' = 2(\frac{1-v_c^2}{E_c} + \frac{1-v_m^2}{E_m})^{-1}.$$

Variables and values used in the calculation of the film thickness in Phantom B and P are listed in the Table 1. The Phantom B parameters were referred to the bovine bone property (Van Buskirk and Ashman, 1981). The PVC parameters in Phantom P were introduced by Li et al. (2015). Loading and grinding wheel motions were estimated from the experimental observation.

Variable (unit)	Name	Values	
		Phantom B	Phantom P
μ_0 (Pa·s)	Dynamic viscosity at standard atmospheric pressure	1.00×10^{-3}	1.00×10^{-3}
r_c (m)	Radius of the grinding wheel	1.25×10^{-3}	1.25×10^{-3}
r_m (m)	Radius of the vessel phantom	2.00×10^{-3}	2.00×10^{-3}
R (m)	Effective radius	7.69×10^{-4}	7.69×10^{-4}
E_c (Pa)	Elastic modulus of the grinding wheel	1.7×10^{11}	1.7×10^{11}
E_m (Pa)	Elastic modulus of the phantom	1.5×10^{10}	2×10^{4}
v_c	Poisson's ratio of the grinding wheel	0.31	0.31
v_m	Poisson's ratio of the phantom	0.11	0.4
E' (Pa)	Effective elastic modulus	2.81×10^{10}	4.76×10^{4}
u_c (m/s)	Grinding wheel rotation linear velocity	20.3	20.3
u_m (m/s)	Grinding wheel orbital linear velocity	1.71	1.71
V (m/s)	Velocity vector	20.4	20.4
w (N)	Normal load	0.163	0.134
W	Dimensionless load	9.78×10^{-6}	4.74
U	Dimensionless velocity	9.45×10^{-10}	5.58×10^{-4}
H (μm)	Minimum film thickness	3.30×10^{-2}	11.9

Table 1: Parameters in film thickness calculation

The film thickness in Phantom B and P during RA is calculated to be 3.3×10^{-2} μm and 11.9 μm, respectively. The grinding wheel abrasive size is mostly under 10 μm as is observed in Figure 3. The abrasives can cut into the bone part in Phantom B but have no contact with Phantom P due to this elastohydrodynamic film.

2.3 Design of Experiment

For each phantom, force in Y direction (Figure 2) was measured at five grinding wheel rotational speeds: 135, 145, 155, 165 and 175 kRPM. Each test was repeated for five times.

3 Results and Discussion

3.1 Force Measurement

Figure 5 shows the measured cyclic grinding force in Phantom B and P at the 135 kRPM rotational speed. The average peak force, denoted as F and indicated in dash line in Figure 5, was calculated by averaging the dominant peaks. Table 2 summarizes the mean and standard deviation (SD) of F at five rotational speeds for Phantom B and P. For each speed and phantom, the 10 SDs are all below 5% of the mean, indicating a strong consistency among five tests.

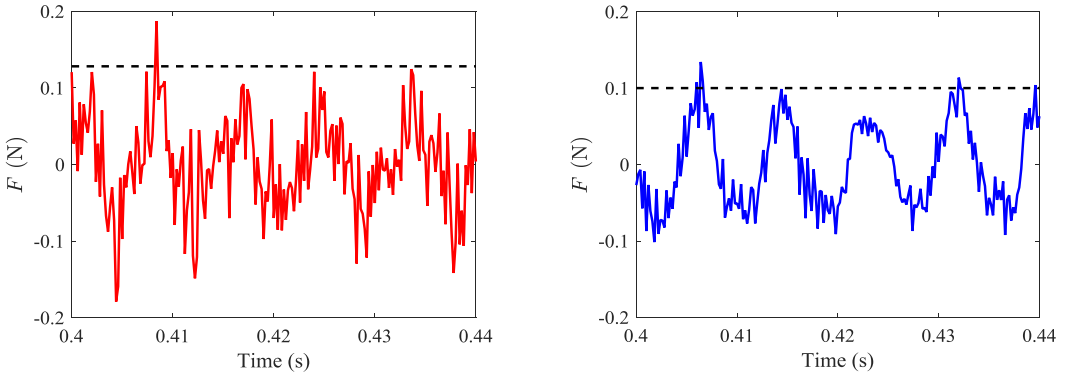

Figure 5: Measured grinding force and the magnitude of average peak force (F) at 135 kRPM rotational speed for Phantoms (a) B and (b) P.

Wheel rotational speed (kRPM)	Phantom	Test 1	Test 2	Test 3	Test 4	Test 5	Mean	SD/ Mean
135	B	0.122	0.127	0.130	0.128	0.136	0.129	3.82%
	P	0.103	0.100	0.10	0.102	0.101	0.101	0.90%
145	B	0.146	0.145	0.148	0.148	0.145	0.146	0.99%
	P	0.119	0.117	0.107	0.106	0.113	0.112	4.95%
155	B	0.163	0.168	0.159	0.159	0.163	0.163	2.20%
	P	0.131	0.134	0.135	0.132	0.135	0.134	1.21%
165	B	0.199	0.202	0.198	0.198	0.204	0.200	1.30%
	P	0.180	0.181	0.180	0.181	0.177	0.180	0.93%
175	B	0.241	0.250	0.245	0.255	0.245	0.247	2.20%
	P	0.208	0.208	0.207	0.215	0.216	0.211	2.16%

Table 2: Force (N) measurement at five rotational speeds in Phantoms B and P.

As shown in Figure 6, the F increased at a higher rotational speed for both Phantoms B and P. The force in Phantom B was larger than that of Phantom P for at a specific rotational speed. The difference in F between Phantoms B and P ranged from 40.9 mN (at 135 kRPM) to 63.3 mN (at 175 kRPM), respectively.

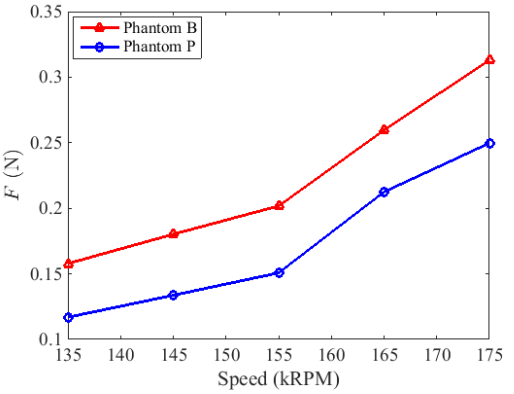

Figure 6: Force magnitudes at five rotational speeds in Phantoms B and P.

3.2 Frequency Analysis and Wheel Motion

Figure 7 shows F in the frequency domain for Phantoms B and P at the grinding wheel rotational speed of 135 kRPM. Based on the grinding wheel motion observed by Zheng et al. (2015), the rotating wheel orbits around the vessel axis and against the inner wall during grinding. In Phantom B (Figure 7(a)), the dominant frequency (117.2 Hz) is the grinding wheel orbital frequency. The frequency of 2,280 Hz is the wheel rotational frequency. In Phantom P (Figure 8(b)), the orbital frequency is 119 Hz and the rotational frequency is 2,280 Hz.

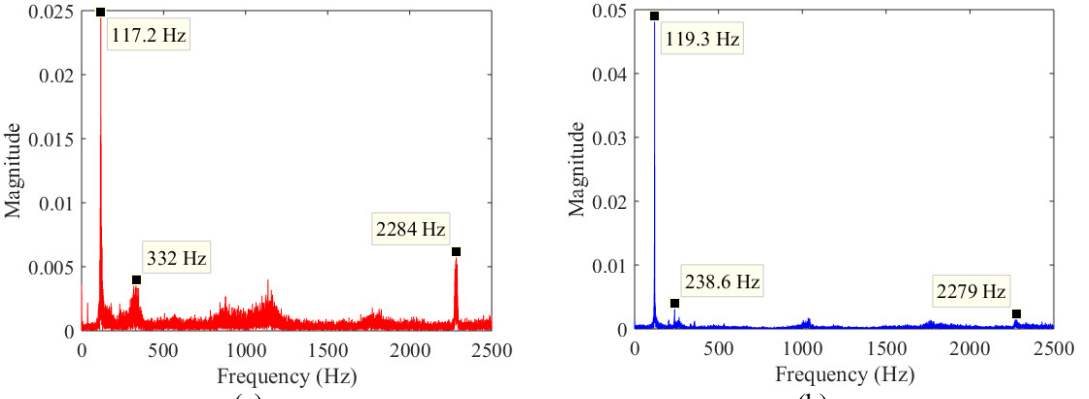

Figure 7: Frequency analysis of grinding force at 135 kRPM for (a) Phantom B and (b) Phantom P.

The orbital frequency at different grinding wheel rotational speed in Phantoms B and P is summarized in Figure 8. For each rotational speed, the orbital frequencies are almost the same for both phantoms. This indicates the same grinding wheel orbital motion and blood mimicking water flow between Phantoms B and P. The orbital frequency increases with the wheel rotational speed. This trend in Figure 8 is similar to that of force in Figure 6. A modeling on the grinding wheel interaction with the blood and vessel wall will be conducted in the future.

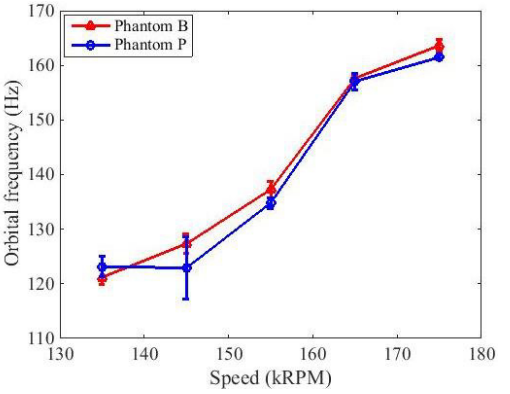

Figure 8: Grinding wheel orbital frequencies at different rotational speeds in phantom B and P.

3.3 Ground Surface

To validate the assumption that Phantom B is ground during RA while Phantom P is not, inner surface morphology of Phantoms B and P before and after RA was examined and compared. The original reamed inner surface of the bone workpiece is shown in Figure 9(a) as the benchmark. Grooves generated by abrasives cutting at the wheel rotational speed of 135 kRPM are observed in Figure 9(b). The groove width is about 10 μm that matches with the abrasive size of the grinding wheel (see Figure 3). No difference was observed between Figures 9(c) and (d), which indicates no grinding occurs in Phantom P. The rough surfaces in Figures 9(c) and (d) were caused by the dip coating process, copying the surface texture of the ground aluminum rod to the inner surface of the PVC vessel phantom.

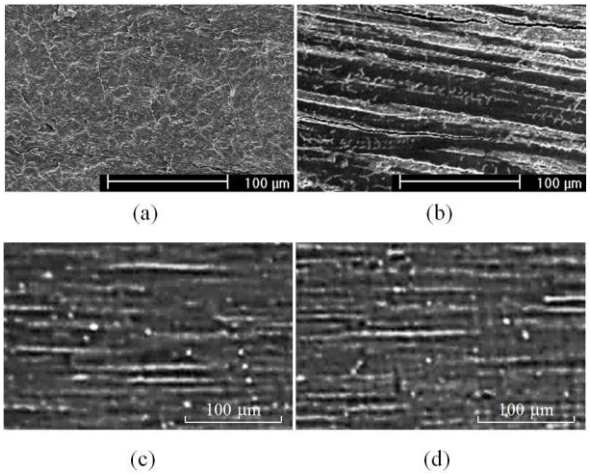

Figure 9: Inner surface morphology (a) pre and (b) post RA in Phantom B and (c) pre and (d) post RA in Phantom P.

4 Conclusions

This paper presented an approach to investigate the RA grinding force based on piezoelectric force dynamometer measurement on two phantoms with and without a ring-bone at the grinding site. Phantom B with the bovine bone workpiece was subject to grinding; while Phantom P with a PVC inner surface was not due to the elastohydrodynamic pressure that lifts the grinding wheel during RA. The force difference between Phantoms B and P in RA was observed ranging from 40.9 to 63.3 mN. Cutting grooves were observed only in Phantom B. Orbital frequencies were same between these two phantoms. This research builds the foundation to study the RA grinding mechanism. Future modeling of the grinding wheel interaction with the blood fluid and the arterial wall will gain better understanding of the RA grinding forces.

References

Barbato E, Carrié D, Dardas P, Fajadet J, Gaul G, Haude M and et al. European expert consensus on rotational atherectomy. *EuroIntervention* 2015; 11(1): 30-36.

Dahdouh Z, Abdel-Massih T, Roule V, Sarkis A and Grollier G. Rotational Atherectomy as endovascular haute couture: a road map of tools and techniques for the interventional management of burr entrapment. *Journal of Interventional Cardiology* 2013; 26(6): 21.

Demer LL, Tintut Y, Vascular calcification: pathobiology of a multifaceted disease, *Circulation* 2008; 117(22): 2938-2948.

Fang G, Ai W, Leeflang S, Duszczyk J and Zhou J. Multipass cold drawing of magnesium alloy minitubes for biodegradable vascular stents. *Material Sci. and Eng*.: C 2013; 33(6): 3481-3488.

Farb A, Roberts DK, Pichard AD, Kent KM andVirmani R. Coronary artery morphologic features after coronary rotational atherectomy: insights into mechanisms of lumen enlargement and embolization. *Am Heart J*. 1995; 129(6): 1058-1067.

Hamrock BJ, Schmid SR and Jacobson BO. *Fundamentals of Fluid Film Lubrication*. Boca Raton: CRC Press, 2004.

Hoffmann R, Mintz G, Kent K, Pichard A, Satler L, Popma J, Hong M, Laird J and Leon M. Comparative early and nine-month results of rotational atherectomy, stents, and the combination of both for calcified lesions in large coronary arteries. *Am J Cardiol.* 1998; 81: 552–557.

Kim MH, Kim HJ, Kim NN, Yoon HS and Ahn SH. A rotational ablation tool for calcified atherosclerotic plaque removal. *Biomed Microdevices* 2011; 13(6): 963-971.

Kini AS, Marmur JD, Duvvuri S, Dangas G, Choudhary S and Sharma SK. Rotational atherectomy: improved procedural outcome with evolution of technique and equipment. single-center results of first 1,000 patients. *Catheterization and Cardiovascular Interventions* 1999; 46(3): 305-311.

Kistler. MiniDyn-multicomponent dynamometer Type 9256C. *Product datasheet* 2003.

Li W, Belmont B and Shih AJ. Design and manufacture of polyvinyl chloride (PVC) tissue mimicking material for needle insertion. In: *Proc. of 43rd North American Manufacturing Research Conference*, 2015.

Lin CP, Wang JH, Lee WL, Ku PM, Yin WH, Tsao TP and Chang CJ. Mechanism and management of burr entrapment: a nightmare of interventional cardiologists. *Journal of Geriatric Cardiology* 2013; 10: 230-234.

Liu Y, Li B, Zheng Y and Shih AJ. Experimental investigation of the speed effect on debris size and surface topography in atherectomy. In: *Proc. of 11th International Conference on Micro Manufacturing*, 2016.

Morii I and Miyazaki S. Current overview of rotational atherectomy. does rotablator make sense? *Emodinamica* 2000; 22: 2-9.

Nakao M, Tsuchiya K, Maeda W and Iijima D. A rotating cutting tool to remove hard cemented deposits in heart blood vessels without damaging soft vessel walls. *CIRP Annals - Manufacturing Technology* 2005; 54(1): 37-40.

National Vital Statistics Report (NVSR). Deaths: final data for 2013. *NVSR* 2014; 64(2): 19-23.

Quevedo HC, Arain SA, Ali G and Rafeh NA. A critical view of the peripheral atherectomy data in the treatment of infrainguinal arterial disease. *J. Invasive Cardiol*. 2014; 26(1): 22-29.

Reifart N, Vandormael M, Krajcar M, Göhring S, Preusler W, Schwarz F, Störger H, Hofmann M, Klöpper J, Müller S and Haase J. Randomized comparison of angioplasty of complex coronary lesions at a single center. Excimer laser, rotational atherectomy, and balloon angioplasty comparison (ERBAC) study. *Circulation* 1997; 96(1): 91-98.

Reisman M, Shuman BJ and Harms V. Analysis of heat generation during rotational atherectomy using different operational techniques. *Cathet. Cardiovasc. Diagn.* 1998; 44(4): 453-455.

Reisman M, Shuman BJ, Dillar D, Fei R, Misser KH, Gordon LS and Harms V. Analysis of low-speed rotational atherectomy for the reduction of platelet aggregation. *Cathet. Cardiovasc. Diagn.* 1998; 45(2): 208-214.

Ritchie JL and Hansen DD. Rotational approaches to atherectomy and thrombectomy. *Z Kardiol*. 1987; 76(Suppl. 6): 59-65.

Safian RD, Feldman T, Muller DW, Mason D, Schreiber T, Haik B, Mooney M and O'Neill WW. Coronary angioplasty and rotablator atherectomy trial (CARAT): immediate and late results of a prospective multicenter randomized trial. *Catheter. Cardiovasc. Interv*. 2001; 53: 213-220.

Van Buskirk WC and Ashman RB. The elastic moduli of bone. *Mechanical Properties of Bone* 1981; 45: 131-143.

Vom Dahl J, Dietz U, Haager PK, Silber S, Niccoli L, Buettner HJ, Schiele F, Thomas M, Commeau P, Ramsdale DR, Garcia E, Hamm CW, Hoffmann R, Reineke T and Klues HG. Rotational atherectomy does not reduce recurrent in-stent restenosis: results of the angioplasty versus

rotational atherectomy for treatment of diffuse in-stent restenosis trial (ARTIST). *Circulation* 2002; 105: 583-588.

Wasiak J, Law J, Watson P and Spinks A. Percutaneous transluminal rotational atherectomy for coronary artery disease. *Cochrane Database Syst Rev*. 2012; 12: CD003334.

Whitlow PL, Bass TA, Kipperman RM, Sharaf BL and et al. Results of the study to determine Rotablator and transluminal angioplasty strategy (STRATAS). *Am. J. Cardiol*. 2001; 87(6): 699-705.

Zheng Y, Belmont B and Shih AJ. Experimental investigation of the grinding wheel dynamics in atherectomy. In: *Proc. of 43rd North American Manufacturing Research Conference*, 2015.